JGR Space Physics

RESEARCH ARTICLE
10.1029/2018JA026193

Key Points:
- Ion drag is the dominant force for driving neutral wind in the SAPS low density region
- The fly-wheel effect gives an active feedback to plasma flow equatorward of SAPS
- Neutral wind feedback amplifies MIT coupling system especially FAC by 20%

Correspondence to:
B. Ferdousi,
bashi@bu.edu

Citation:
Ferdousi, B., Nishimura, Y., Maruyama, N., & Lyons, L. R. (2019). Subauroral neutral wind driving and its feedback to SAPS during the 17 March 2013 geomagnetic storm. *Journal of Geophysical Research: Space Physics*, *124*, 2323–2337. https://doi.org/10.1029/2018JA026193

Received 26 OCT 2018
Accepted 20 JAN 2019
Accepted article online 28 JAN 2019
Published online 28 MAR 2019

Subauroral Neutral Wind Driving and Its Feedback to SAPS During the 17 March 2013 Geomagnetic Storm

Banafsheh Ferdousi[1,2], Yukitoshi Nishimura[1,3], Naomi Maruyama[4], and Larry R. Lyons[1]

[1]Department of Atmospheric and Oceanic Sciences, University of California at Los Angeles, Los Angeles, CA, USA, [2]Center for Space Physics and Department of Astronomy, Boston University, Boston, MA, USA, [3]Center for Space Physics and Department of Electrical and Computer Engineering, Boston University, Boston, MA, USA, [4]National Oceanic and Atmospheric Administration (NOAA), Space Weather Prediction Center (SWPC), Boulder, CO, USA

Abstract Subauroral Polarization Streams (SAPS) are associated with closure of region 2 field-aligned current (R2 FAC) through the low conductivity region. Although SAPS have often been studied from a magnetosphere-ionosphere coupling perspective, recent observations suggest strong interaction also exists between SAPS and the thermosphere. Our study focuses on thermospheric wind driving and its impact on SAPS and R2 FAC during the 17 March 2013 geomagnetic storm using both observations and the physics-based Rice Convection Model-Coupled Thermosphere, Ionosphere, Plasmasphere, electrodynamics (RCM-CTIPe) model that self-consistently couples the magnetosphere-ionosphere-thermosphere system. Defense Meteorological Satellite Program (DMSP)-18 and Gravity Field and Steady-State Ocean Circulation Explorer (GOCE) satellite observations show that, as the storm progresses, sunward ion flows intensify and expand equatorward and are accompanied by strengthening of subauroral neutral winds with some delay. Our model successfully reproduces time evolution and overall structure of the sunward ion drift and neutral wind. A force term analysis is performed to investigate the momentum transfer to the neutrals from the ions. Contrary to previous studies showing that Coriolis force is the main driver of neutrals during storm time, we find that the ion drag is the largest force driving westward neutral wind in the SAPS region where the ion density is low in the trough region. Furthermore, simulations with and without the neutral wind dynamo effect are compared to quantify the effect of the neutral to plasma flow. The comparison shows that the self-consistent active ionosphere thermosphere coupling increases the R2 FAC and the westward ion drift equatorward of the SAPS region by 20% and 40% by the flywheel effect, respectively.

1. Introduction

Subauroral Polarization Streams (SAPS) are intense northward electric field driving sunward plasma convection at the dusk-premidnight subauroral region (Foster & Vo, 2002) and inner magnetosphere (Nishimura et al., 2008; Puhl-Quinn et al., 2007). SAPS contribute to ionospheric composition changes (Anderson et al., 1991; Karlsson et al., 1998), midlatitude troughs (Anderson et al., 1991; Foster et al., 2007; Spiro et al., 1978), storm-enhanced density plumes (Foster et al., 2014, 2007; Foster & Rideout, 2007; Zou et al., 2013), and enhance ion upflows (X. Zhang et al., 2017), as well as the dynamics of the plasmasphere and plasmapause (e.g., Goldstein et al., 2005). SAPS are more prominent during geomagnetic active time, but SAPS during both quiet and moderately disturbed conditions have also been reported by a recent statistical study by Kunduri et al. (2017) based on Super Dual Auroral Radar Network. These phenomena become stronger and move to lower latitudes with increasing geomagnetic activity based on both observation and simulation (e.g., Foster & Vo, 2002; Gkioulidou et al., 2011, 2009; Lyons et al., 2009).

They are believed to be formed by the necessity for closing the downward region 2 field-aligned currents (R2 FACs), which are generated by the increased ring current pressure gradient, through the low-conductivity region that lies equatorward of the electron plasma sheet. In this scenario, the magnetosphere acts as a current generator to maintain a large electric field gradient that is formed in the SAPS events (Anderson et al., 2001).

While SAPS have often been discussed within the magnetosphere-ionosphere coupling framework, recent studies of subauroral neutral wind observations have shown existence of a strong interaction with the thermosphere. Neutral winds in the midlatitude and low-latitude thermosphere are disturbed during magnetically active times since Joule heating and ion drag deposited in the auroral zone drive neutral wind surges and changes in the global circulation (e.g., Fuller-Rowell et al., 1994). Enhanced westward winds are found to peak around the same latitude as SAPS flows from comparisons between ion drift and neutral wind measurements (Wang et al., 2011, 2012). Different forces have been suggested to explain the acceleration of neutral wind, involving, for example, the ion drag force in the aurora zone (Wang et al., 2018) and on a global scale (Wang et al., 2012), the Coriolis force (Lühr et al., 2007; S.-R. Zhang et al., 2015), and pressure gradient.

Furthermore, the wind disturbances last longer than magnetospheric driving forces due to their large inertia (called the flywheel effect; Deng et al., 1993; Lyons et al., 1985; Odom et al., 1997; Richmond et al., 2003). The flywheel effect is generated by the wind disturbances that have previously been accelerated by storm time convection via ion drag or auroral heating. At midlatitude and low latitude, the process to generate electric fields that are generated by disturbed winds are called the disturbance dynamo. The main driver of the disturbance dynamo process is the enhancement of the westward wind at midlatitude that is driven by the Coriolis force (Blanc & Richmond, 1980). However, it is difficult to observationally investigate the causality by quantifying force terms that contribute to accelerating the neutral wind in the SAPS region because of difficulties in measuring the force terms. Utilizing physics-based models is necessary not only to quantify momentum exchange for driving subauroral neutral wind but also to evaluate the level of the feedback process to the ionosphere and magnetosphere due to the flywheel effect. This motivated us to perform a study on the storm time thermospheric wind effect on the ionospheric plasma drift associated with SAPS. This study provides for the first time characterization and evaluation of the midlatitude flywheel effect and its role in the inner magnetosphere and atmosphere-ionosphere coupling system feeding back the magnetosphere. We also perform force term analysis to evaluate which forces are responsible for accelerating neutral wind toward the direction of plasm flow.

In this study, we use data from Defense Meteorological Satellite Program (DMSP)-18 and Gravity Field and Steady-State Ocean Circulation Explorer (GOCE) satellite during the St. Patrick's Day storm event of 2013 caused by an Interplanetary Coronal Mass Ejection. This storm has been chosen since it was relatively strong (DST ~ −130 nT) during the latest solar cycle 24, and SAPS activity has been documented previously for this storm (Foster et al., 2014; Raeder et al., 2016; Yu et al., 2015; S.-R. Zhang et al., 2015). We also use a physics-based model of the coupled magnetosphere-ionosphere-thermosphere system that self-consistently couples Rice Convection Model (RCM; Toffoletto et al., 2003; Wolf, 1983) and Coupled Thermosphere, Ionosphere, Plasmasphere, electrodynamics (CTIPe) model (e.g., Fuller-Rowell et al., 2002; Millward et al., 2001). The coupled model includes the electrodynamic coupling and interactions and feedback between the inner magnetosphere and ionosphere-thermosphere system (Maruyama et al., 2011).

The second section describes our methodology and tools used for this study. The third section focuses on our result, identifying SAPS from DMSP measurements and comparing it to neutral wind measurement from GOCE. We then perform observation and simulation comparison to verify our model results and investigate the effects of different forces on driving neutral wind as well as the effect of neutral wind feedback into the ionosphere and magnetosphere system. Finally, we summarize and give our conclusions in the last section.

2. Methodology

2.1. Observation

2.1.1. DMSP

The DMSP satellites measure precipitating electrons and ions, ion density, cross-track ion drifts, and magnetic field. The DMSP satellites are in Sun-synchronous, nearly circular polar orbits at ~800-km altitude nearly in the dawn-dusk meridian. The SSJ electrostatic analyzer measures electrons and ions from 32 eV to 30 keV in 20 logarithmically placed steps every second (Hardy et al., 1984). The SSIES instrument contains a scintillation monitor and drift meter for measuring the density and cross-track drift every second (Rich & Hairston, 1994). The magnetic field is obtained by the SSM instrument with 1-s resolution (Rich et al., 1985).

2.1.2. GOCE

The GOCE satellite measured the neutral density and cross-track neutral wind in the thermosphere on a ~90-min orbit (96.5° inclination) from 2009 to 2013 (Bruinsma et al., 2014). The GOCE orbital plane is fixed to the Sun (06 and 18 local times) ~260-km altitude. The neutral density and cross-track winds are obtained from the accelerometer onboard the spacecraft using the rate of satellite acceleration due to the atmospheric drag and known parameters (satellite mass, cross section, drag coefficient, and satellite speed).

2.1.3. DMSP and GOCE Conjugation

During this event, DMSP-18 and GOCE had very good conjugacy in the dusk sector (magnetic local time [MLT] ~ 18.5–20) which is our primary region of interest. We also compare data on the dawnside to investigate the dawn-dusk asymmetry, although their locations were slightly different (DMSP at MLT ~ 9 and GOCE at MLT ~ 7). In this study, DMSP measurements of plasma density, precipitating electron energy flux, magnetic field, and ion velocity at altitude ~830 km are used. GOCE provides measurements of neutral wind density and cross-track velocity at altitude ~270 km.

2.2. The Coupled RCM-CTIPe Model

The coupled RCM-CTIPe model is composed of three well-developed and tested physical models: (1) the CTIPe model (Fuller-Rowell et al., 1996; Millward et al., 2001, 1996); (2) the RCM (Toffoletto et al., 2003; Wolf, 1983); and (3) the global electrodynamic solver based on the National Center for Atmospheric Research Thermosphere-Ionosphere Electrodynamics General Circulation Model (NCAR-TIEGCM) (Richmond & Maute, 2014). The model includes the electrodynamic coupling, interactions, and feedback between the inner magnetosphere and the thermosphere-ionosphere-magnetosphere system. It also includes the ring current and the auroral-zone distribution of ionospheric currents and FACs associated with high latitude convection that connects the ionosphere and magnetosphere, as well as ionospheric wind-generated dynamo current sources. It is able to describe high latitude convection and corotation electric fields and the storm time processes including prompt penetration, disturbance dynamo and SAPS, all of which are crucial in calculating the storm time electric field in the ionosphere and magnetosphere, and Joule heating and ion drag that are the main drivers of the storm time neutral wind. The detailed description of the model coupling can be found in Maruyama et al. (2011). The horizontal resolution of the electrodynamic solver (variable in latitude with minimum 0.69° in the subauroral region, with longitude resolution of 4.5°) is high enough to resolve the fine structure of the R2 FACs and the corresponding SAPS latitudinal features. In this study, in order to improve the consistency of the location between R2FAC and auroral ionospheric conductance, the calculation of the auroral ionization caused by the diffuse aurora (the type of aurora caused by the particles that are scattered by plasma waves into the loss cone without the aid of additional energy) in RCM has newly been implemented in the CTIPe model, since the conductivity can greatly alter the ionospheric convection electric field including SAPS.

2.2.1. Model Input

The global electric field in the coupled model critically depends on the spatial and temporal variation of the polar cap potential, which is driven by solar-wind-magnetosphere interaction. The convection pattern poleward of the RCM domain is given by Heelis et al. (1982). The polar cap potential drop used to drive the RCM was initially calculated from 5-min averages of Advanced Composition Explorer solar wind and interplanetary magnetic field data using the empirical relations of Boyle et al. (1997) but modified so that if the potential drop exceeds 150 kV, the potential is reduced linearly to saturate at 200 kV based on DMSP measurements (Hairston et al., 2003).

The Hilmer and Voigt (1995) model has been adopted for the magnetic field and time-dependent polar cap boundary (RCM high latitude boundary). Another input of the model is the plasma sheet outer boundary condition (density and temperature), which is estimated from the Tsyganenko and Mukai (2003) statistical model. The plasma sheet input is important since higher temperature and smaller density in the plasma sheet leads to reduced shielding and enhanced penetration of electric field equatorward of the inner boundary of electron precipitation (Garner et al., 2004; Spiro et al., 1988).

Auroral precipitation patterns are obtained by combining RCM precipitation within the RCM domain and the TIROS/NOAA satellite-based model driven by the hemispheric power index (Fuller-Rowell & Evans, 1987) poleward of the RCM domain. The model forcing is updated every 12 min. It is important to note that the disturbance dynamo electric field is self-consistently calculated in the model (Fuller-Rowell et al., 2002). Upward propagating tides from the lower atmosphere represent an additional input as described by Millward et al. (2001). We use solely the semidiurnal (2,2) tidal component specified at the lower boundary of the model, with a prescribed magnitude of 300 m with a phase of the maximum at 0100 LT, since the (2,2) mode is the crucial tidal mode for reproducing the diurnal variation of the vertical $E \times B$ drift at the magnetic equator.

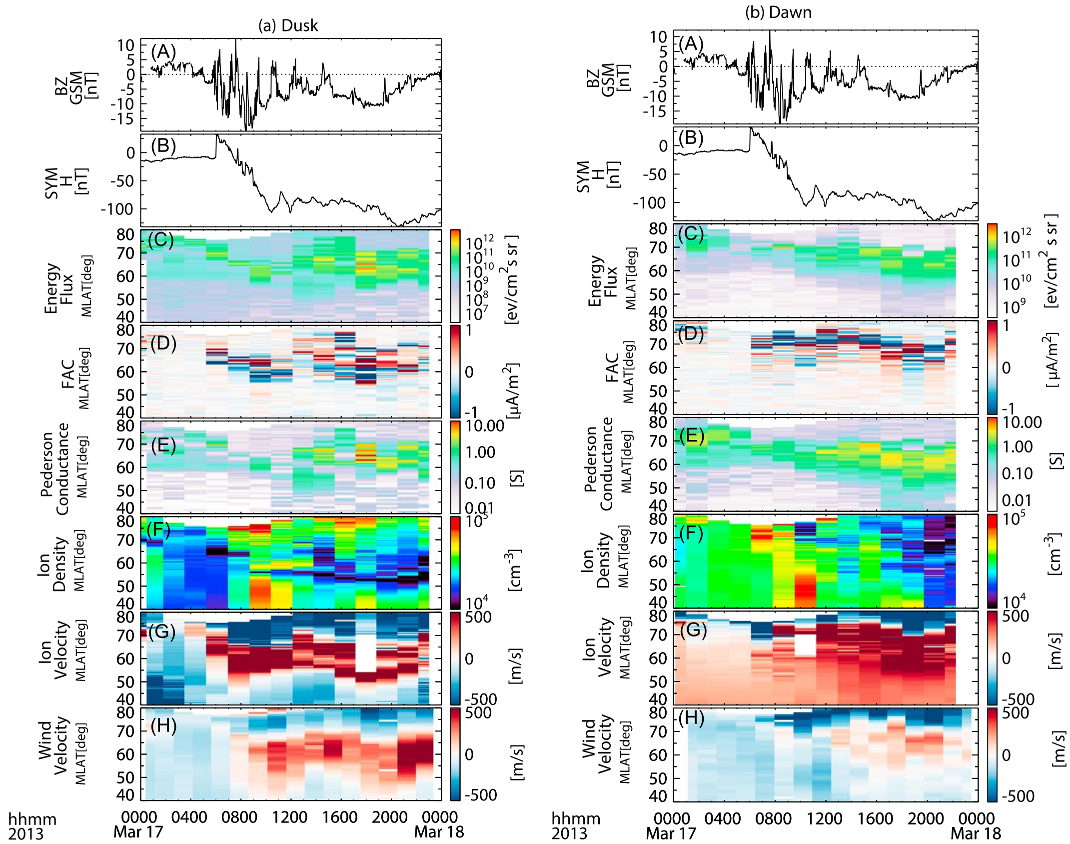

Figure 1. The correlation between Subauroral Polarization Streams from DMSP 18 and neutral wind from GOCE during St. Patrick's Day geomagnetic storm of 2013. (a) Dusk (both DMSP and GOCE at MLT = 18.5 to 20) and (b) dawn (DMSP at MLT = 9 and GOCE at MLT = 7). The panels from top to bottom present: (A) IMF B_z from OMNI, (B) SYM-H, (C) electron precipitation, (D) FAC, (E) Pederson conductance, (F) ion density, (G) sunward ion drift from DMSP, and (H) neutral wind from GOCE. The *y* axis in panels (C) to (H) show the latitude from 40° to 80°, each vertical band presents 90-min orbit of DMSP and GOCE. FAC = field-aligned current; DMSP = Defense Meteorological Satellite Program; GOCE = Gravity Field and Steady-State Ocean Circulation Explorer.

3. Results

3.1. Observations

Figure 1 shows correlation between the measured sunward plasma flow from DMSP and neutral wind from GOCE at dusk (Figure 1a) and dawn (Figure 1b). Panel (A) shows IMF B_z in Geocentric coordinate systems from the OMNI data set. IMF B_z first fluctuated between south and north and then turned southward (at ~6 UT) and stayed mostly southward until ~20 UT. Finally, it slowly turned northward toward the end of this time interval. SYM-H in panel (B) fell after the storm sudden commencement around 6:00 UT and reached −100 nT around 10:00 UT when IMF B_z became strongly negative. Then it stayed nearly steady until 20 UT when it dropped again to −130 nT, indicating double dips during the main phase of this storm. Panels (C) to (H) show the magnetic latitude distribution of DMSP observations on each orbit (every ~90 min). Panel (C) is precipitating electron energy flux, and the FAC determined from the DMSP magnetometer (positive upward) is shown in panel (D). Panel (E) presents the Pederson conductance determined using the Robinson formula (Robinson et al., 1987) based on the electron energy flux, and plasma density from DMSP is shown in panel (F). The last two panels show the ion drift and neutral wind velocities from the DMSP and GOCE satellites. The positive direction is sunward (red), which is westward at dusk and eastward at dawn.

As shown in Figure 1a, as the storm progresses, the electron precipitating flux increases, and the auroral oval expands equatorward. The R2 FAC extends well equatorward of the auroral oval in the subauroral low conductivity region where the midlatitude trough has formed. The sunward ion drift has two latitudinally bifurcated bands particularly after ~12 UT. The equatorward portion of the flow can be identified as SAPS since it is located equatorward of the electron precipitation and within the trough. The FAC and SAPS velocity show

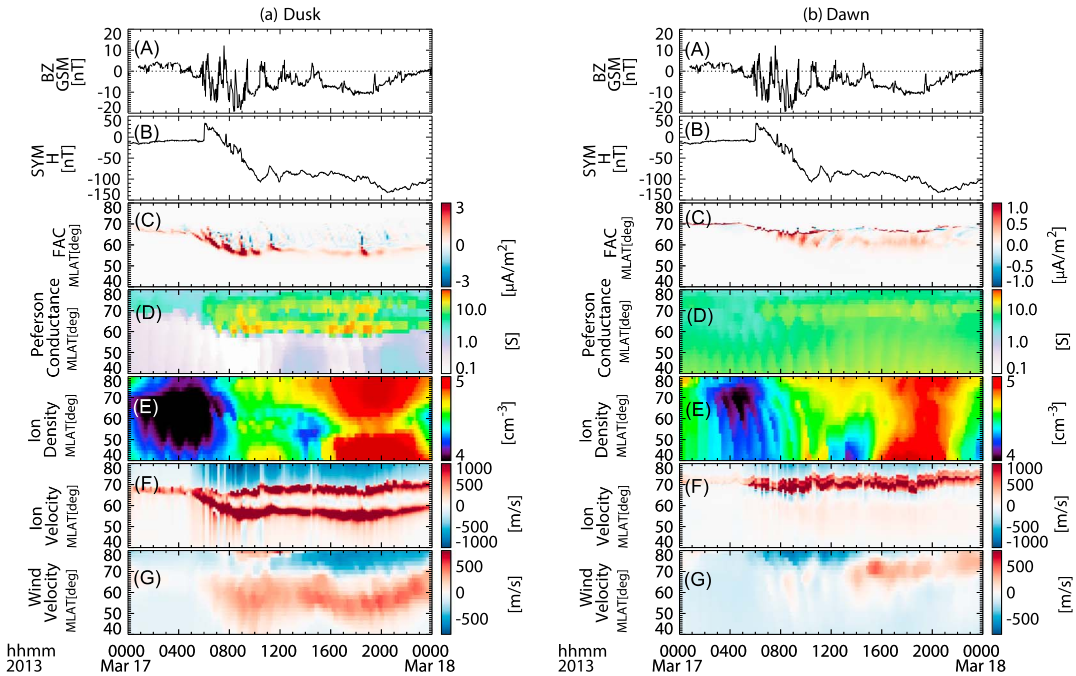

Figure 2. The correlation between Subauroral Polarization Streams and neutral flows from the coupled Rice Convection Model-Coupled Thermosphere, Ionosphere, Plasmasphere, electrodynamics model during St. Patrick's Day geomagnetic storm of 2013. (a) Dusk (MLT = 20) and (b) dawn (MLT = 9). The panels from top to bottom present: (A) IMF B_Z from OMNI, (B) SYM-H, (C) FAC, (D) Pederson conductance, (E) density, (F) sunward ion drift velocity, and (G) neutral wind. FAC = field-aligned current.

a two-dip structure (equatorward expansion at ~8 and ~20 UT), similar to the SYM-H dips. Observations from GOCE during the same time period show that the neutral wind response resembles the plasma flow with approximately 2-hr time delay consistent with previous studies at subauroral and middle latitudes (S.-R. Zhang et al., 2015). Since the orbits of DMSP and GOCE are roughly 90 min, it is hard to determine exact timing of the neutral's acceleration in response to ions.

In contrast, at the dawn side (Figure 1b), all parameters show equatorward motion as the storm progresses, although the two-dip structure was not clearly seen. The sunward ion drift is as intense as on the duskside, but the flow magnitude peak was located in the oval (~68° latitude). The sunward winds are much weaker than that of the dusk side.

3.2. Simulation

Figure 2 shows a comparison of the ion drift and neutral wind velocities and their corresponding quantities at (Figure 2a) dusk (20 MLT) and (Figure 2b) dawn (9 MLT) from the coupled RCM-CTIPe model. From top to bottom, panels are (A) IMF B_Z, (B) SYM-H, (C) FAC, (D) Pederson conductance, (E) density (at the same altitude as DMSP ~ 800 km), (F) ion velocity (~300 km, same as for wind; the ion velocity only slightly changes in altitude because of equipotential along field lines), and (G) neural wind velocity at the same altitude as GOCE (~300 km). Our simulation successfully reproduces the SAPS structure, timing, and magnitude by comparing to the observations in Figure 1a. The main feature of the SAPS, the double band structure, is evident in the plasma drift plot (Figure 2a(F)). Also, the two dips of SAPS latitudinal structure around 8 UT and 20 UT are consistent with that of the observations. The neutral wind enhances about an hour after westward flow velocity enhances, and it reaches ~500 m/s at dusk. The double dips are also seen in the neutral wind (Figure 2a(G)). Similarly, reasonable agreement is obtained between the observations and model results at the dawn side (Figures 1b and 2b). The neutral wind is much weaker than on the dusk and comparable to the observation.

Figure 3 presents a more detailed comparison between observation (red solid line) and simulation during the storm (blue solid line) and, for reference, quiet time (black dashed line) of drift velocity at different times

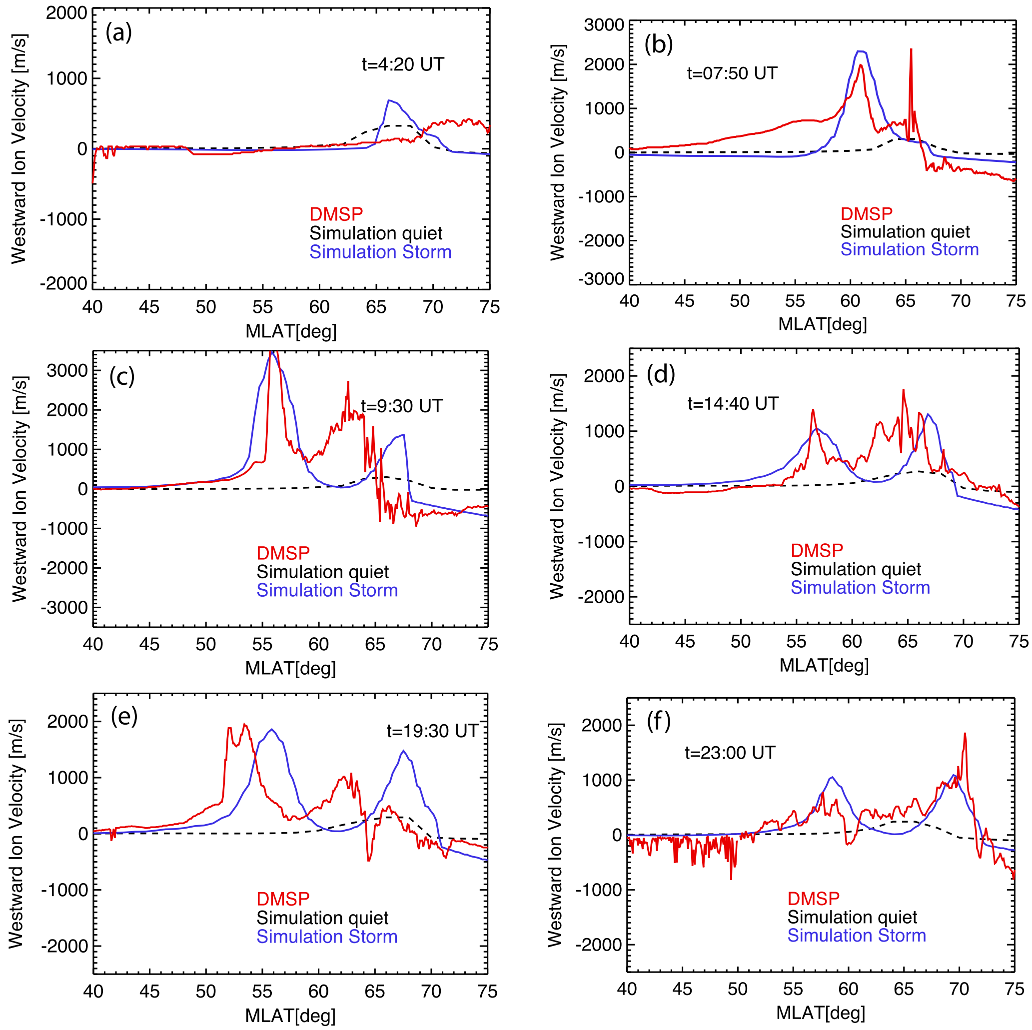

Figure 3. Observation and simulation comparison of ion drift velocity from DMSP (red) and storm time simulation (blue) and quiet time simulation (black dashed line) at 20 MLT. The sudden sharp drop of at 68° is due to Rice Convection Model high latitude boundary. Panels (a)–(f) present different times (before, during, and during recovery of the storm). DMSP = Defense Meteorological Satellite Program.

(before, during, and during recovery of the storm). A constant offset of −200 m/s exists before the storm in DMSP flow velocity, which may be due to instrumental effects, and this value has been subtracted from all panels of Figure 3. For the quiet time, the polar cap potential value was kept constant at a pre-storm level for the entire simulation (polar cap potential = 25 kV). In addition, the magnetospheric magnetic field is kept constant at the values at 00UT on 17 March 2013, and the aurora precipitation (energy flux and average energy) is kept at the quiet time level (TIROS activity level = 7.4 [GW]). The first plot is for a couple of hours before the storm, during which the sunward flow in both simulation and observation is weak and comparable to the quite time simulation. The sunward flow enhances after the storm onset (07:50 UT), and at 9:30 UT, the double bands are formed around 56° and 66° magnetic latitude in the simulation and 56° and 63° in observation. The westward flows remain strong at ~2,000 m/s, and the double bands remain prominent during the second dip of the storm (Figures 3d-3e). The location, magnitude, and latitudinal extent of the simulated and measured ion drift are mostly captured by the simulation throughout the storm. However, there exists some inconsistencies between observation and simulation. These inconsistencies might be due to a couple of reasons. The RCM uses the centered dipole instead of International Geomagnetic Reference Field (IGRF), and thus, effects of the internal magnetic field are not precisely described in the RCM. The location (in MLT) of DMSP changes between passes between 18.5

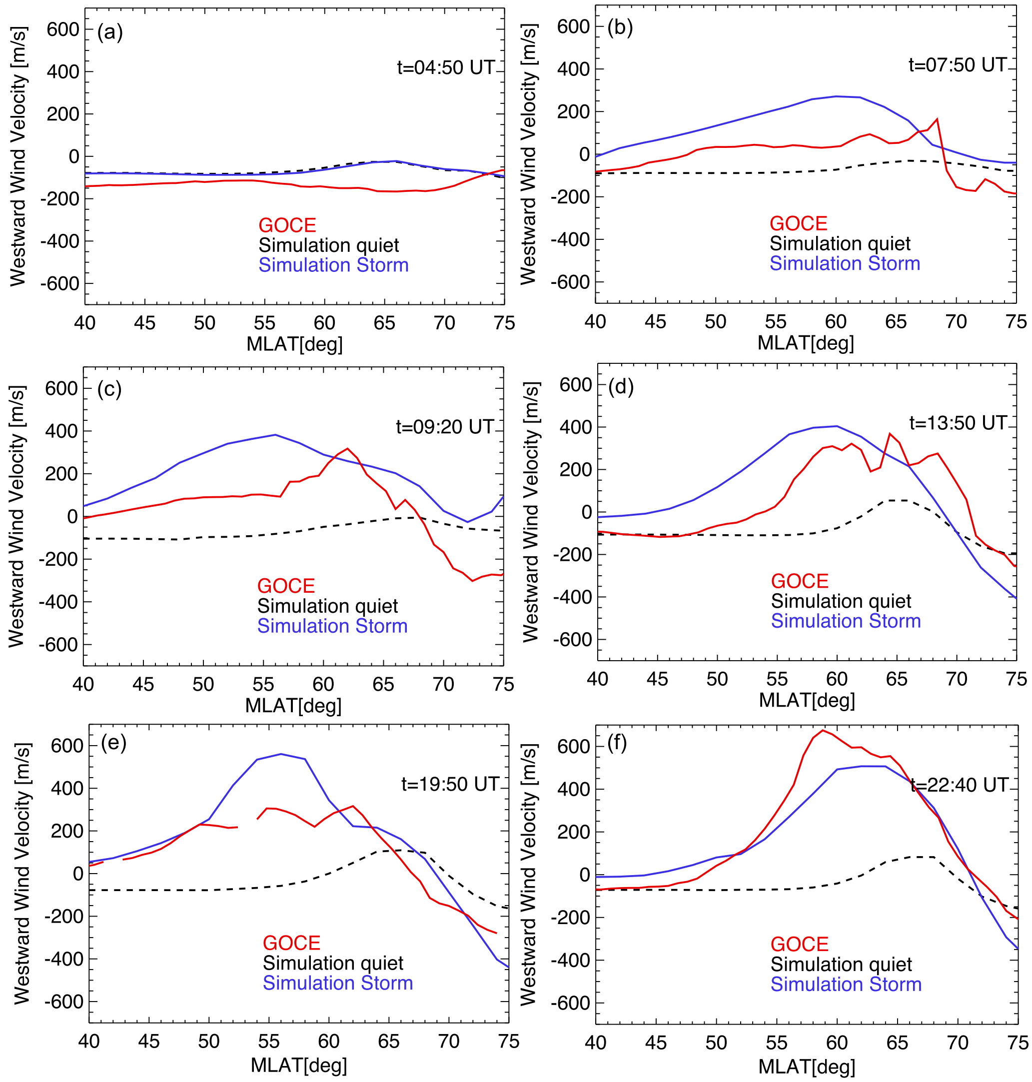

Figure 4. Observation and simulation comparison of westward wind velocity from GOCE (red) and storm time simulation (blue) and quiet time simulation (black dashed line) at 20 MLT. The geographic longitude was determined at 55 magnetic latitude. Panels (a)–(f) present different times (before, during, and during recovery of the storm). GOCE = Gravity Field and Steady-State Ocean Circulation Explorer.

and 20 MLT, but we use fixed MLT (MLT = 20) for simplicity. The CTIPe longitudinal resolution (18°) is not sufficiently high to obtain simulation results exactly at the satellite locations. Finally, the small structures in the observation are not captured by the simulation since the simulation uses smoothed auroral precipitation, polar cap potential, and plasma sheet boundary input. As mentioned in section 2.2.1, those are specified by statistical models and are not necessarily accurate for the particular event. Nevertheless, the model has successfully reproduced the key ionosphere-thermosphere features in the subauroral region for this event.

Figure 4 presents the comparison of westward neutral wind between observation (red), simulation of storm (blue), and simulation of quiet time (dashed black) at different times (before, during, and recovery of the storm). Before the storm (4:50 UT), the wind is weak and very comparable to quiet time. As the storm progresses, the westward wind velocity increases from almost zero up to several hundred meters per second with the maximum values at high latitude where most of the Joule heating has been deposited. The wind enhancement smoothly extends to midlatitude where the wind enhancement is collocated with the ion drift increase associated with SAPS during the main phase of the storm. The wind however remains enhanced even during the recovery phase of the storm when the ion drift velocity decreases (cf. Figures 3f and 4f).

The wind enhancement during the recovery phase plays an important role in generating the flywheel effect and will be discussed in further detail in the following sections. The overall feature of the simulated wind enhancement is remarkably consistent with the observation, but there still exist some inconsistencies between model and simulation. Some of the reasons have been discussed in the previous paragraph.

3.2.1. Force Term Analysis

In order to understand how the neutral wind is driven, we evaluate the contribution of each force term. For this purpose, we use the equation of motion that describes the force balance of neutral gas

$$\frac{\partial}{\partial t}\mathbf{U}_{\mathrm{n}} = \nu_{\mathrm{ni}}(\mathbf{V}_{\mathrm{i}}-\mathbf{U}_{\mathrm{n}}) - 2\Omega\times\mathbf{U}_{\mathrm{n}} - (\mathbf{U}_{\mathrm{n}}\cdot\nabla)\mathbf{U}_{\mathrm{n}} - \frac{1}{\rho}\nabla P + \frac{1}{\rho}\nabla(\mu\nabla\mathbf{U}_{\mathrm{n}}), \tag{1}$$

where $\mathbf{V}_i$ and $\mathbf{U}_n$ are plasma velocity and neutral velocity, respectively, ν_{ni} is neutral-ion collision frequency, P is neutral gas pressure, ρ is gas mass density, $\mathbf{\Omega}$ is angular rotation rate of Earth, and μ is the coefficient of the sum of turbulence and the molecular viscosity (Fuller-Rowell et al., 1996). The gravity term can be neglected in equation (1) since the model assumes that it is independent of altitude over the model altitude region (80 to ~600 km) based on the shallow atmosphere approximation. From left to right, the main forces that are acting on neutral gas in equation (1) are ion drag, Coriolis, advection, pressure gradient, and viscosity. When the plasma interacts with the neutral gas, the ion drag force acts and can accelerate neutral to high velocity in the presence of electric field. The Coriolis force is formed as a result of motion of the atmosphere, which is clockwise in the northern hemisphere when viewed from above. The advection term is formed as a result of gradient or change in neutral velocity. The pressure gradient is formed as a result of Joule heating, absorption of solar radiation, or tidal, planetary, and gravity waves propagating from the lower atmosphere. The viscosity works to smooth out the gradient in neutral velocity, which is mainly effective in the vertical direction over short distance.

Figure 5 shows a comparison of sunward plasma velocity, neural wind, and the forces acting on them at dusk (Figure 5a) and dawn (Figure 5b), positive sunward. The first four panels (A–D) of Figure 5 are repetition of Figure 2, but the ion drift has been regridded on the geographic frame of CTIPe from the magnetic frame of the RCM. The overall time evolution of the ion drift is the same as in Figure 2, but the two-band structure is less evident due to the coarser grids of CTIPe thermosphere module (2° × 18°). The ion drift below 50° latitude shows antisunward flows near the peaks of the two dips of the storms. The last six panels (E–J) present the difference between ion drift velocity and neutral wind, ion drag, Coriolis, horizontal advection, pressure gradient forces, and Joule heating. The viscous term effect was negligible, so it is not included in the figure. As described in the previous section, the neural wind enhances westward within 2 hr of plasma drift enhancement.

The difference between the ion drift velocity and neutral wind is intense (>500 m/s) in the SAPS region where the density is low. As a result, the ion drag force (first term in equation (1)) enhances within the same location as the westward plasma enhancement and forms prior to neutral wind acceleration. Thus, ions accelerate neutrals in the direction of the plasma flow. The Coriolis force also develops in this region, but it is stronger during the second dip of the storm, and its contribution is not as large as the ion drag. This is consistent with the earlier finding by Blanc and Richmond (1980), where the Coriolis force takes several hours to develop due to transport from the nightside auroral latitudes. The horizontal advection acts against the other forces above 58° magnetic latitude (Figure 5a(H)). This force however acts in the favor of westward movement below 58° magnetic latitude, and it is more dominant at the two dips of the storm when there is intensification and changes in drift velocity. The pressure gradient is smaller than the ion drag, and it was sunward during the first dip of the storm and antisunward during the second dip (Figure 5a(I)). The fluctuations in the pressure gradient is caused mainly by the changes in the Joule heating (Figure 5a(J)).

The sunward (eastward) plasma flows, neutral wind, and their corresponding forces at dawn are shown in Figure 5b as a contrast. The plasma flow is enhanced at 70° latitude within the auroral oval. However, there is no substantial plasma flow enhancement in the subauroral region on the dawn side. The neutral wind, however, is weak at dawn, similar to the observations. The ion drag force is also dominant below 70° latitude at dawn, but it is essentially balanced with the day-to-night pressure gradient and the Coriolis terms. Thus, the wind acceleration is not effective at this local time but occurs at earlier local times. As shown in Figure 6g, the wind acceleration occurs at postmidnight by the ion drag and pressure gradient. This difference in the forces explains the dawn-dusk asymmetry in the neutral wind.

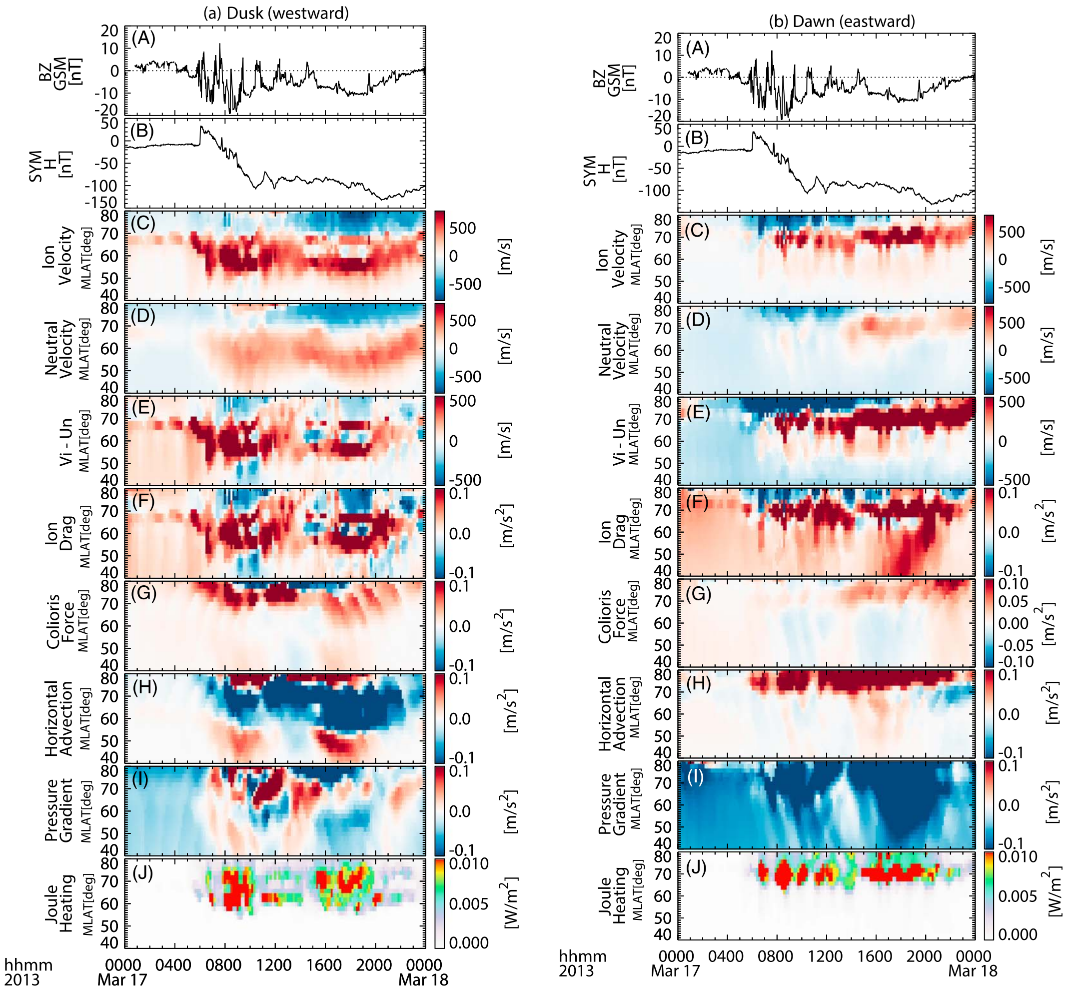

Figure 5. Simulation of force term analysis in sunward direction at dusk (a) and at dawn (b). (from top to bottom) (A) IMF B_z, (B) SYM-H, (C) ion drift velocity, (D) neutral wind velocity, (E) difference between ion velocity and neutral ($\mathbf{V}_i$-$\mathbf{U}_n$), (F) ion drag, (G) Coriolis force, (H) horizontal advection, (I) pressure gradient, and (J) Joule heating. The flows and forces are positive sunward.

Polar views of the simulated sunward forces are given in Figures 6 and 7 at two times: in the middle of the first main phase at 8 UT when the IMF B_z is southward and near the end of the first main phase at 9:30 UT when IMF B_z briefly turns northward. For the blue-to-red color maps, the sunward and antisunward components are in red and blue, respectively. The green and magenta arrows indicate the plasma drift and neutral wind velocity, respectively. At first time interval (8 UT, Figure 6), the ion drift has strong westward motion in the midlatitude region where the plasma trough forms (Figures 6a and 6c). The midlatitude plasma trough and its formation has been previously studied (e.g., Rodger, 2008). Comparing the forces, the ion drag force is the strongest within the SAPS region in comparison to the Coriolis and horizontal advection. These forces are mainly effective at auroral and subauroral latitudes. The pressure gradient term is weakly positive on the nightside while negative (antisunward) on the dayside.

At 9:30 UT when IMF B_z turns northward and becomes close to zero (Figure 7), the double-band structure of the drift velocity is formed and evident at dusk-premidnight region. The ion drift becomes very slow at low latitudes (less than ~45°), while the neutral wind is still strong (magenta arrows) at premidnight. The ion drag force and the velocity difference between $\mathbf{V}_i$ and $\mathbf{U}_n$ become negative in this region (Figures 7d and 7e). The antisunward ion drag force is also evident in Figure 5a(E and F) from 9 UT to 11 UT. Around this time, the neutral wind, which has large inertia, is exerting force on ions and driving them toward sunward. This is the flywheel effect that has previously been observed in the high latitude of the ionosphere (Deng et al., 1993; Lyons et al., 1985). Our study is the first to reproduce the flywheel effect in the midlatitude

10.1029/2018JA026193

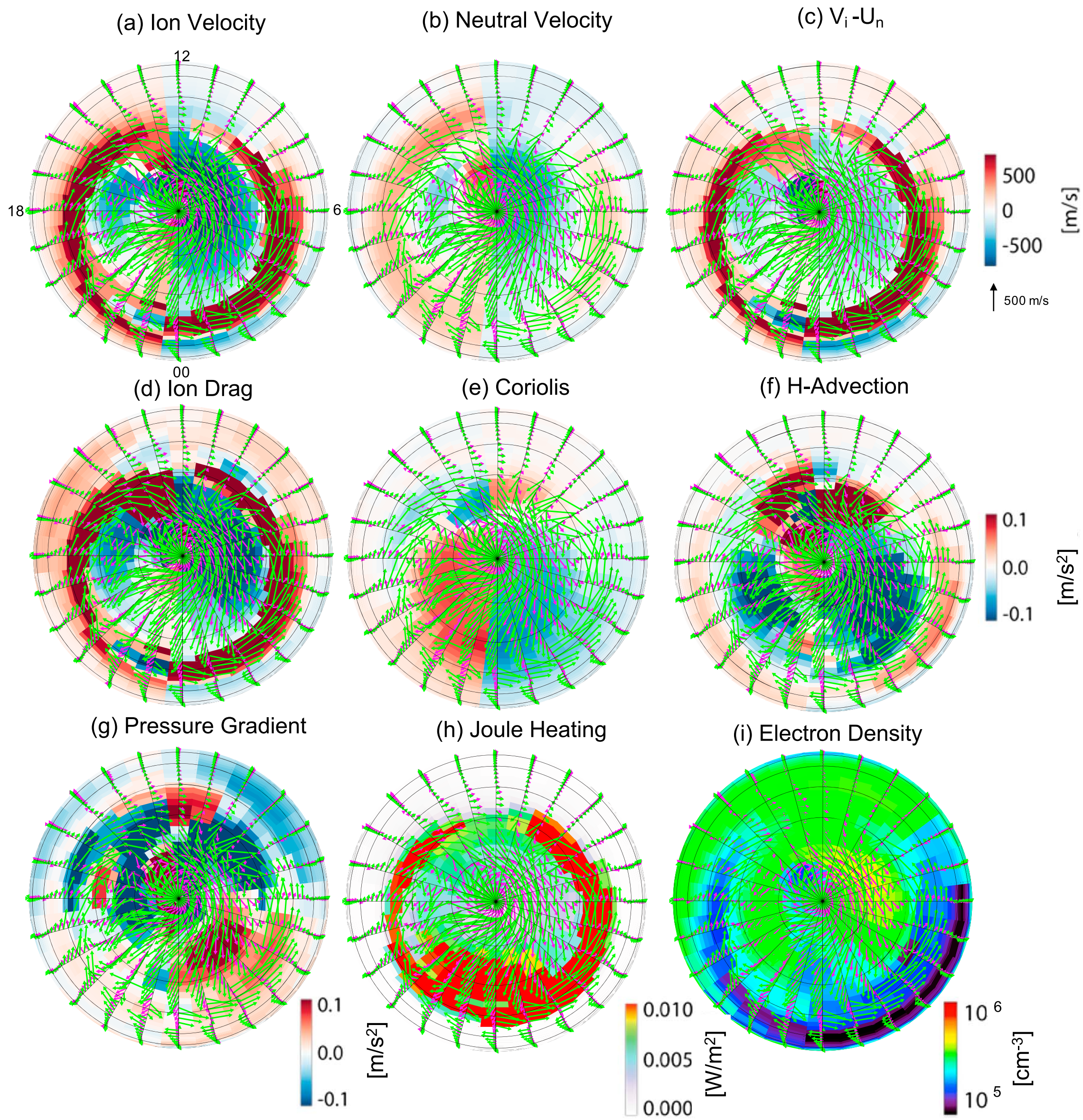

Figure 6. Polar view simulation of force term analysis in southward direction at 8 UT (a) ion drift velocity, (b) neutral wind velocity, (c) electron density, (e) $\mathbf{V}_i$-$\mathbf{U}_n$, (f) ion drag, (g) Coriolis force, (h) horizontal advection, (i) pressure gradient, and (j) Joule heating. The sun is located at top. Each solid circle presents magnetic latitude with 10° increment.

region by physics-based models. The electron density increased at 9:30 UT compared to 8 UT though the trough configuration still exists. The main reason is that equatorward wind pushes plasma to a higher altitude where the recombination is slower (the old positive phase at midlatitudes; e.g., Prölss, 1997). The thermal expansion might also cause increase in the electron density (e.g., Fedrizzi et al., 2008).

Figure 8 presents the same quantities as Figures 5 but in the southward direction. The plasma drift above 60° latitude in the nightside was intense at 8 UT but weakened and moved toward lower latitude by 20 UT. The neutral wind has almost the same pattern as does the drift but extends over a wider magnetic latitude extent. The forces that dominate in the southward direction at dusk are the ion drag and horizontal advection. The Coriolis force and pressure gradient act against the ion drag below 60° latitude with a similar magnitude. This explains the small neutral wind magnitude in the subauroral region. The southward Coriolis force is formed as a result of westward ion velocity enhancement as shown by comparison between Figures 5c and 8g.

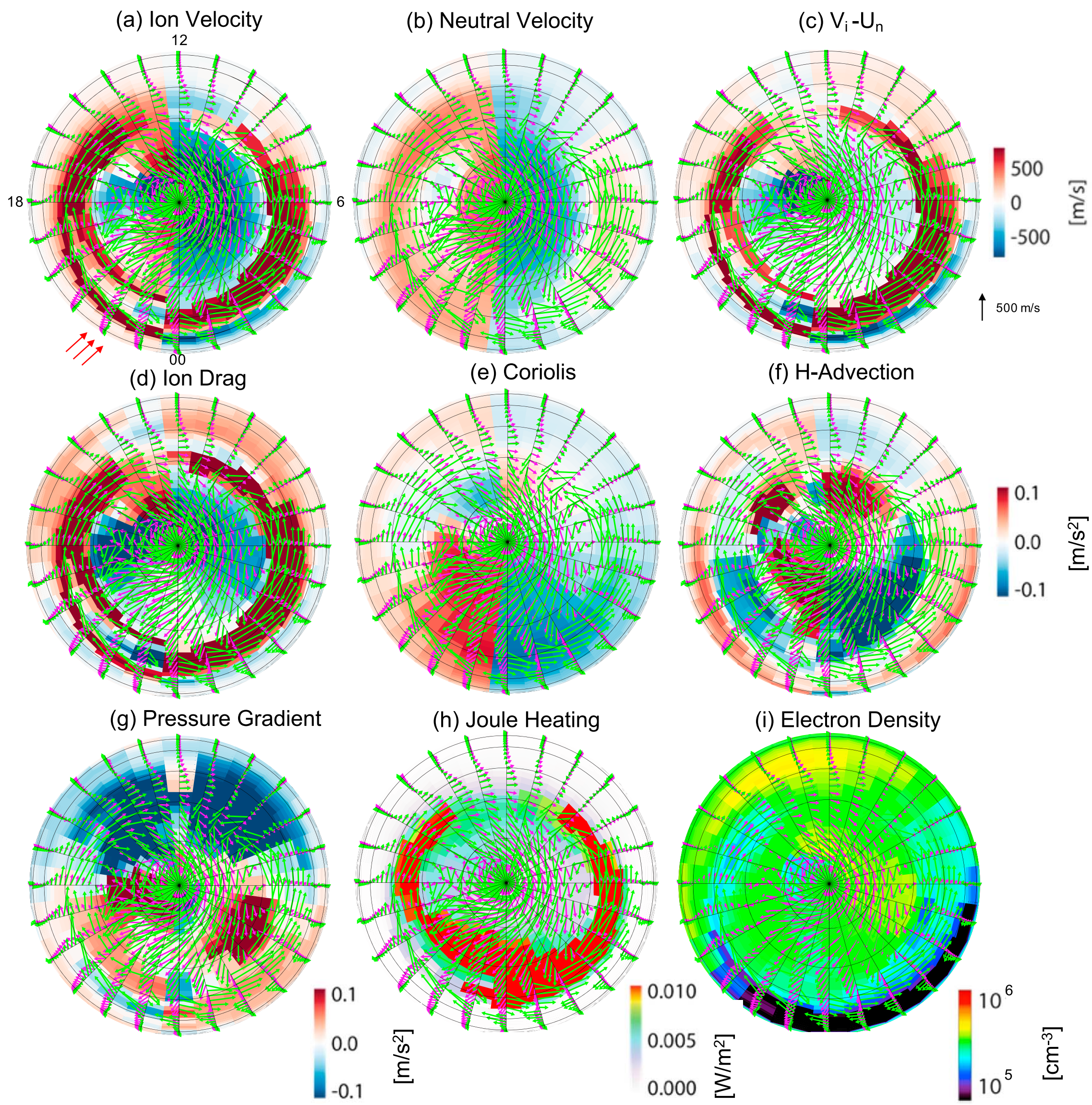

Figure 7. Same as Figure 6 but for 9:30 UT.

In the dawn sector (9 MLT), the neutral wind is enhanced in the southward direction near the two dips of the storm, and the most dominant force is the equatorward pressure gradient that shows repetitive equatorward propagation. This is caused by enhanced Joule heating (due to elevated ion drift and precipitation) that intensifies the equatorward pressure gradient. The repetitive pressure gradient is likely related to fluctuations in the IMF B_Z, which modulates the high-latitude forcing (seen as quasiperiodic drift and Joule heating). The equatorward propagation of the pressure gradient corresponds to the equatorward neutral wind surges created by the enhanced joule heating (e.g., Bruinsma & Fedrizzi, 2012; Fuller-Rowell et al., 1994). The resultant enhanced equatorward wind contributes to slow development of the westward Coriolis force seen in Figure 5g (Blanc & Richmond, 1980).

3.2.2. Wind Feedback Effects to the Ionosphere and Magnetosphere (Flywheel Effects)

In order to study the effect of neutral wind on magnetosphere-ionosphere- thermosphere coupling, we performed a second simulation without the neutral wind feedback to the ionosphere. Figures 9a–9c show the comparison between these runs for the FAC, the westward plasma drift, and the electric potential, respectively. Panel (B) shows a run with self-consistent calculation of the wind-generated electric field, (C) without the wind feedback, (D) the difference (with feedback minus without feedback) between these runs, and (E)

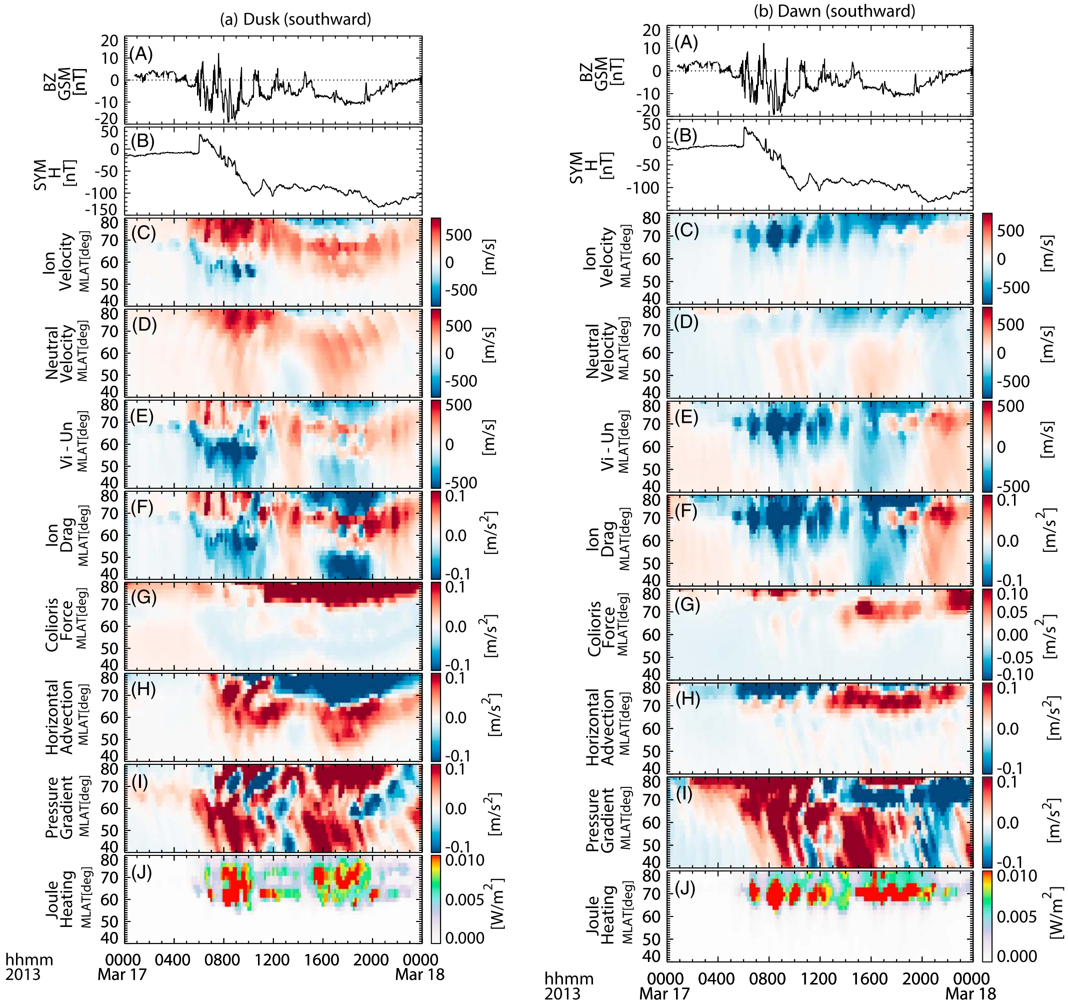

Figure 8. Simulation of force term analysis in southward direction at dusk (a) and at dawn (b). (from top to bottom) (A) IMF B_z, (B) SYM-H, (C) ion drift velocity, (D) neutral wind velocity, (E) $\mathbf{V}_i$-$\mathbf{U}_n$, (F) ion drag, (G) Coriolis force, (H) horizontal advection, (I) pressure gradient, and (J) Joule heating.

and corresponding percentage difference. Figures 9a and 9b show that the downward R2 FAC and SAPS flows are larger for the run with the wind feedback. The ion drift also extends to latitudes lower than the SAPS region. While this drift is substantially weaker than that within the SAPS region, it is still significant (~few hundred meters per second) and is ~20–40% stronger when wind feedback is included (Figure 9b(A and B)). The ion drag force increases the ion drift in the direction of the neutral wind (westward), meaning a larger poleward electric field. The electric field driven by neutral wind feedbacks to the magnetosphere and increases the transport of the ring current particles which penetrate to lower latitudes. As a result, R2 FAC gets stronger and enhanced closer to the earth, enhancing the electric field in the lower latitudes which then further increases the ion drift. When the wind feedback was included in our run, the FAC increased by 20% (maximum around 55° latitude) and the westward ion velocity enhanced in the subauroral zone (45° to 55°) by 40%, compared to the run without wind feedback. We also could describe the feedback from the wind to the SAPS using the Ohm's law ($J = \sigma\,(\mathbf{E} + \mathbf{U}_n \times \mathbf{B})$). To maintain the poleward Pedersen current that connects R1 and R2 FACs, the wind effect ($\mathbf{U}_n \times \mathbf{B}$) requires a larger electric field ($E_\perp$). A larger electric field results in a more enhanced ring current and also R2 FACs. This thus increases the closing Pedersen current. The larger Pedersen current should be closed by $\mathbf{U}_n \times \mathbf{B}$ and $E_\perp$. But the larger $E_\perp$ leads to a larger $\mathbf{U}_n$ via ion drag, thus requiring an even larger $E_\perp$. This is a positive feedback loop, giving the larger FAC and electric field in the presence of the wind feedback shown in Figure 9. The energy is not conserved between the ionosphere electric field and wind, but the

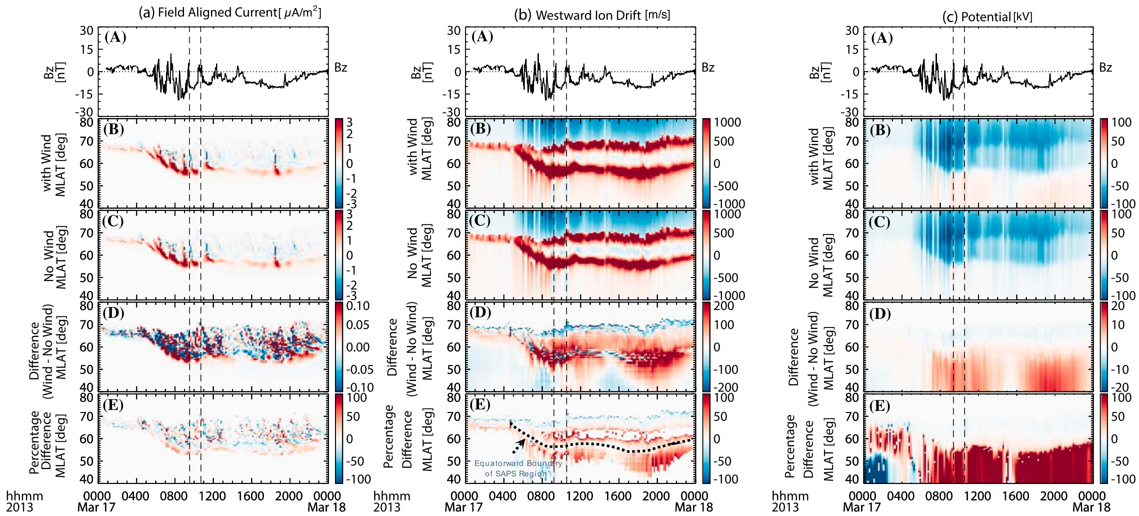

Figure 9. Comparison of simulation runs with/without neutral wind feedback. (a) Field-aligned current and (b) ion drift and (c) potential: (A) IMF BZ wind (B) feedback is included, (C) without wind, (D) difference (Wind – No Wind), and (E) difference between simulation runs in percentage. The two dashed line indicate the two overshielding events when IMF B_Z turns northward.

magnetosphere energy (pressure gradient that supplies the R2 FAC and solar wind-magnetosphere dynamo that supplies R1 FAC) changes depending on the electric field in the system.

Two periods under the overshielding conditions are clearly identified at 9:00 and 10:30 UT in Figure 9b(B and C) as eastward ion drift below ~55° magnetic latitude. These timings correspond to the IMF northward turnings and the reduction in ion drift near the open-closed boundary. The overshielding electric fields did not propagate latitudinally but emerged and disappeared simultaneously across latitude. These findings suggest that the overshielding electric fields are caused by reduction in the R1 FAC system while the R2 FAC system has been well-developed after the ring current particles have had enough time to reconfigure themselves in response to the solar wind driving (e.g., Ebihara et al., 2008; Kikuchi et al., 2010), rather than the disturbance dynamo effect that slowly propagates from high to low latitudes as equatorward winds develop.

Figure 9b(E) shows that the percentage difference in westward drift at ~52–55° MLAT during the overshielding conditions is weaker, meaning that the overshielding electric field (eastward drift) for the run with the wind feedback is stronger. This enhanced overshielding feature is more pronounced for the second period (10:30 UT) when the wind had more time to respond to the storm. Our result is consistent with the previous study by Peymirat et al. (1998) where they showed that wind effect increases the north-south electric field (east-west drift) in the auroral zone while decreasing the east-west electric field (north-south drift) equatorward of the auroral zone. The wind feedback effect changes the electric field with the same signs as the overshielding process caused by R2 FAC and thus including the wind feedback effect in fact enhances the overshielding.

4. Summary and Conclusions

Observation from DMSP and GOCE and the coupled CTIPe-RCM model was used to study the relation between neutral wind and ion drift in the SAPS region during the St. Patrick's storm in 2013. The simulation successfully reproduced the overall structure and timing of the SAPS and wind. A force term analysis was performed to evaluate the effects of different forces on driving neutrals in the SAPS region. We also studied the effect of wind feedback in the magnetosphere and ionosphere coupling system. The main outcomes of this paper are summarized here.

1. The location and time variation of the forces indicate that the ion drag force dominantly accelerates the neutrals in the direction of the SAPS flow. The equatorward component of the wind may be primarily due to horizontal advection, with some contribution from the Coriolis force. The pressure gradient that was formed as a result of Joule heating acts mostly against the other forces.

2. The neutral winds exhibit the flywheel effect equatorward of the SAPS peak velocity, accelerating ions to the westward direction for 2 hr when the IMF B_z becomes close to zero.
3. Wind feedback has strong effect on magnetosphere-ionosphere-thermosphere coupling processes, increasing the FAC by in average 20% leading to enhancement of electric field. As a result, the ion drift penetrates toward lower latitudes and increase in average by 40% by overshielding.

Acknowledgments
This work was supported by NASA grants NNX17AL22G, 80NSSC18K0657, NNX16AB83G, NNX15AI91G, 80NSSC17K0720, and 80NSSC17K0718; NSF grants PLR-1341359, AGS-1737823, AGS-1452298, AGS-1552248; and AFOSR FA9559-16-1-0364 and FA9550-18-1-0483. We thank support from the CEDAR workshop “Grand Challenge: Multi scale I-T system dynamics” and the previous “Grand challenge: Storms and Substorms Without Border”. DMSP and GOCE data were obtained online (cedar.openmadrigal.org) and (earth.esa.int/web/guest/missions/esa-operational-missions/goce/goce-thermospheric-data). The authors would like to thank Tim Fuller-Rowell for his helpful discussions and his expert guidance on implementing RCM precipitation into CTIPe model. We would like to acknowledge high performance computing support from Cheyenne provided by NCAR's Computational and Information Systems Laboratory. Data from the model simulations used in this study are available online (https://scholar.colorado.edu/cires_facpapers/78).

References

Anderson, P. C., Carpenter, D. L., Tsuruda, K., Mukai, T., & Rich, F. J. (2001). Multisatellite observations of rapid subauroral ion drifts (SAID). *Journal of Geophysical Research*, *106*, 29,585–29,599. https://doi.org/10.1029/2001JA000128

Anderson, P. C., Heelis, R. A., & Hanson, W. B. (1991). The ionospheric signatures of rapid subauroral ion drifts. *Journal of Geophysical Research*, *96*, 5785–5792. https://doi.org/10.1029/90JA02651

Blanc, M., & Richmond, A. (1980). The ionospheric disturbance dynamo. *Journal of Geophysical Research*, *85*, 1669–1686. https://doi.org/10.1029/JA085iA04p01669

Boyle, C. B., Reiff, P. H., & Hairston, M. R. (1997). Empirical polar cap potentials. *Journal of Geophysical Research*, *102*(A1), 111–125.

Bruinsma, S. L., Doornbos, E., & Bowman, B. R. (2014). Validation of GOCE densities and thermosphere model evaluation. *Advances in Space Research*, *54*(4), 576–585. https://doi.org/10.1016/j.asr.2014.04.008

Bruinsma, S. L., & Fedrizzi, M. (2012). Simultaneous observations of TADs in GOCE, CHAMP and GRACE density data compared with CTIPe, AGU Fall Meeting Abstr., 2012, SA33B-05.

Deng, W., Killeen, T. L., Burns, A. G., Roble, R. G., Slavin, J. A., & Wharton, L. E. (1993). The effects of neutral inertia on ionospheric currents in the high-latitude thermosphere following a geomagnetic storm. *Journal of Geophysical Research*, *98*(A5), 7775–7790. https://doi.org/10.1029/92JA02268

Ebihara, Y., Nishitani, N., Kikuchi, T., Ogawa, T., Hosokawa, K., & Fok, M.-C. (2008). Two-dimensional observations of overshielding during a magnetic storm by the Super Dual Auroral Radar Network (SuperDARN) Hokkaido radar. *Journal of Geophysical Research*, *113*, A01213. https://doi.org/10.1029/2007JA012641

Fedrizzi, M., Fuller-Rowell, T. J., Codrescu, M., Maruyama, N., & Khalsa, H. (2008). Sources of *F*-region height changes during geomagnetic storms at mid-latitudes. In P. M. Kintner, Jr., A. J. Coster, T. J. Fuller-Rowell, A. J. Mannucci, M. Mendillo, & R. Heelis (Eds.), *Midlatitude ionospheric dynamics and disturbances, Geophysical Monograph Series* (Vol. 181, pp. 247–258). Washington, DC: American Geophysical Union. https://doi.org/10.1029/181GM22

Foster, J. C., Erickson, P. J., Coster, A. J., Thaller, S., Tao, J., Wygant, J. R., & Bonnell, J. W. (2014). Storm time observations of plasmasphere erosion flux in the magnetosphere and ionosphere. *Geophysical Research Letters*, *41*, 762–768. https://doi.org/10.1002/2013GL059124

Foster, J. C., & Rideout, W. (2007). Storm enhanced density: magnetic conjugacy effects. *Annales Geophysicae*, *25*, 1791–1799.

Foster, J. C., Rideout, W., Sandel, B., Forrester, W. T., & Rich, F. J. (2007). On the relationship of SAPS to storm-enhanced density. *Journal of Atmospheric Space Terrestrial Physics*, *69*(3), 303–313. https://doi.org/10.1016/j.jastp.2006.07.021

Foster, J. C., & Vo, H. B. (2002). Average characteristics and activity dependence of the subauroral polarization stream. *Journal of Geophysical Research*, *107*(A12), 1475. https://doi.org/10.1029/2002JA009409

Fuller-Rowell, T. J., Codrescu, M. V., Moffett, R. J., & Quegan, S. (1994). Response of the thermosphere and ionosphere to geomagnetic storms. *Journal of Geophysical Research*, *99*, 3893–3914. https://doi.org/10.1029/93JA02015

Fuller-Rowell, T. J., & Evans, D. S. (1987). Height-integrated Pedersen and Hall conductivity patterns inferred from the TIROS/NOAA satellite data. *Journal of Geophysical Research*, *92*, 7606–7618. https://doi.org/10.1029/JA092iA07p07606

Fuller-Rowell, T. J., Rees, D., Quegan, S., Moffett, R. J., Codrescu, M. V., & Millward, G. H. (1996). A coupled thermosphereionosphere model (CTIM). In R. W. Schunk (Ed.), *STEP: Handbook of ionospheric models* (pp. 239–279). Boulder, CO: Science Communication on Solar-Terrestrial Physics.

Fuller-Rowell, T. M., Millward, G. H., Richmond, A. D., & Codrescu, M. V. (2002). Storm-time changes in the upper atmosphere at low latitudes. *Journal of Atmospheric and Solar - Terrestrial Physics*, *64*(12-14), 1383–1391. https://doi.org/10.1016/S1364-6826(02)00101-3

Garner, T. W., Wolf, R. A., Spiro, R. W., Burke, W. J., Fejer, B. G., Sazykin, S., et al. (2004). Magnetospheric electric fields and plasma sheet injection to low L-shells during the 4–5 June 1991 magnetic storm: Comparison between the Rice Convection Model and observations. *Journal of Geophysical Research*, *109*, A02214. https://doi.org/10.1029/2003JA010208

Gkioulidou, M., Wang, C.-P., & Lyons, L. R. (2011). Effect of self-consistent magnetic field on plasma sheet penetration to the inner magnetosphere: Rice convection model simulations combined with modified Dungey force-balanced magnetic field solver. *Journal of Geophysical Research*, *116*, A12213. https://doi.org/10.1029/2011JA016810

Gkioulidou, M., Wang, C.-P., Lyons, L. R., & Wolf, R. A. (2009). Formation of the Harang reversal and its dependence on plasma sheet conditions: Rice convection model simulations. *Journal of Geophysical Research*, *114*, A07204. https://doi.org/10.1029/2008JA013955

Goldstein, J., Sandel, B. R., Forrester, W. T., Thomsen, M. F., & Hairston, M. R. (2005). Global plasmasphere evolution, 22– 23 April 2001. *Journal of Geophysical Research*, *110*, A12218. https://doi.org/10.1029/2005JA011282

Hairston, M. R., Hill, T. W., & Heelis, R. A. (2003). Observed saturation of the ionosphereic polar cap potential during the 31 March 2001 storm. *Geophysical Research Letters*, *30*(6), 1325. https://doi.org/10.1029/2002GL015894

Hardy, D. A., Schmitt, L. K., Gussenhoven, M. S., Marshall, F. J., Yeh, H. C., Shumaker, T. L., & Pantazis, J. (1984). Precipitating electron and ion detectors (SSJ/4) for the block 5D/flights 6–10 DMSP satellites: Calibration and data presentation, Rep. AFGL-TR-84-0317, Air Force Geophys. Lab., Hanscom Air Force Base, Bedford, MA.

Heelis, R. A., Lowell, J. K., & Spiro, R. W. (1982). A model of the high-latitude ionospheric convection pattern. *Journal of Geophysical Research*, *87*, 6339–6345. https://doi.org/10.1029/JA087iA08p06339

Hilmer, R. V., & Voigt, G.-H. (1995). A magnetospheric magnetic field model with flexible current systems driven by independent physical parameters. *Journal of Geophysical Research*, *100*, 5613–5626. https://doi.org/10.1029/94JA03139

Karlsson, T., Marklund, G. T., Blomberg, L. G., & Mälkki, A. (1998). Subauroral electric fields observed by the Freja satellite: A statistical study. *Journal of Geophysical Research*, *103*, 4327–4341. https://doi.org/10.1029/97JA00333

Kikuchi, T., Ebihara, Y., Hashimoto, K. K., Kataoka, R., Hori, T., Watari, S., & Nishitani, N. (2010). Penetration of the convection and overshielding electric fields to the equatorial ionosphere during a quasiperiodic *DP* 2 geomagnetic fluctuation event. *Journal of Geophysical Research*, *115*, A05209. https://doi.org/10.1029/2008JA013948

Kunduri, B. S. R., Baker, J. B. H., Ruohoniemi, J. M., Thomas, E. G., Shepherd, S. G., & Sterne, K. T. (2017). Statistical characterization of the large-scale structure of the subauroral polarization stream. *Journal of Geophysical Research: Space Physics*, *122*, 6035–6048. https://doi.org/10.1002/2017JA024131

Lühr, H., Rentz, S., Ritter, P., Liu, H., & Häusler, K. (2007). Average thermospheric wind patterns over the polar regions, as observed by CHAMP. *Annales de Geophysique*, *25*(5), 1093–1101. https://doi.org/10.5194/angeo-25-1093-2007

Lyons, L. R., Killen, T. L., & Walterscheid, R. L. (1985). The neutral wind "fly wheel" as a source of quiet time polar cap currents. *Geophysical Research Letters*, *12*, 101–104. https://doi.org/10.1029/GL012i002p00101

Lyons, L. R., Wang, C.-P., Gkioulidou, M., & Zou, S. (2009). Connections between plasma sheet transport, region 2 currents, and entropy changes associated with convection, steady magnetospheric convection periods, and substorms. *Journal of Geophysical Research*, *114*, A00D01. https://doi.org/10.1029/2008JA013743

Maruyama, N., Fuller-Rowell, T. J., Codrescu, M. V., Anderson, D., Richmond, A. D., Maute, A., et al. (2011). Modeling the storm time electrodynamics. In M. Abdu & D. Pancheva (Eds.), *Aeronomy of the Earth's atmosphere and ionosphere*, *IAGA Special Sopron Book Series* (Vol. *2*). Dordrecht: Springer. https://doi.org/10.1007/978-94-007-0326-1_35

Millward, G. H., Müller-Wodarg, I. C. F., Aylward, A. D., Fuller-Rowell, T. J., Richmond, A. D., & Moffett, R. J. (2001). An investigation into the influence of tidal forcing on *F* region equatorial vertical ion drift using a global ionosphere-thermosphere model with coupled electrodynamics. *Journal of Geophysical Research*, *106*, 24,733–24,744. https://doi.org/10.1029/2000JA000342

Millward, G. H., Rishbeth, H., Fuller-Rowell, T. J., Aylward, A. D., Quegan, S., & Moffett, R. J. (1996). Ionospheric F_2 layer seasonal and semiannual variations. *Journal of Geophysical Research*, *101*, 5149–5156. https://doi.org/10.1029/95JA03343

Nishimura, Y., Wygant, J., Ono, T., Iizima, M., Kumamoto, A., Brautigam, D., & Friedel, R. (2008). SAPS measurements around the magnetic equator by CRRES. *Geophysical Research Letters*, *35*, L10104. https://doi.org/10.1029/2008GL033970

Odom, C. D., Larsen, M. F., Christensen, A. B., Anderson, P. C., Hecht, J. H., Brinkman, D. G., et al. (1997). ARIA II neutral flywheel-driven field-aligned currents in the postmidnight sector of the auroral oval: A case study. *Journal of Geophysical Research*, *102*(A5), 9749–9759. https://doi.org/10.1029/97JA00098

Peymirat, C., Richmond, A. D., Emery, B. A., & Roble, R. G. (1998). A magnetosphere-thermosphere-ionosphere electrodynamics general circulation model. *Journal of Geophysical Research*, *103*, 17,467–17,477. https://doi.org/10.1029/98JA01235

Prölss, G. W. (1997). Magnetic storm associated perturbations of the upper atmosphere. In B. T. Tsurutani, W. D. Gonzales, Y. Kamide, & J. K. Arballo (Eds.), *Magnetic storms*, *Geophysical Monograph 98* (pp. 183–202). Washington, DC: American Geophysical Union. https://doi.org/10.1029/GM098p0227

Puhl-Quinn, P. A., Matsui, H., Mishin, E., Mouikis, C., Kistler, L., Khotyaintsev, Y., et al. (2007). Cluster and DMSP observations of SAID electric fields. *Journal of Geophysical Research*, *112*, A05219. https://doi.org/10.1029/2006JA012065

Raeder, J., Cramer, W. D., Jensen, J., Fuller-Rowell, T., Maruyama, N., Toffoletto, F., & Vo, H. (2016). Sub-auroral polarization streams: A complex interaction between the magnetosphere, ionosphere, and thermosphere. *Journal of Physics: Conference Series*, *767*, 012021. https://doi.org/10.1088/1742-6596/767/1/012021

Rich, F., & Hairston, M. (1994). Large-scale convection patterns observed by DMSP. *Journal of Geophysical Research*, *99*, 3827. https://doi.org/10.1029/93JA03296

Rich, F. J., Hardy, D. A., & Gussenhoven, M. S. (1985). Enhanced ionosphere-magnetosphere data from the DMSP satellites. *Eos, Transactions American Geophysical Union*, *66*(26), 513. https://doi.org/10.1029/EO066i026p00513

Richmond, A. D., Lathuille're, C., & Vennerstroem, S. (2003). Winds in the high-latitude lower thermosphere: Dependence on the interplanetary magnetic field. *Journal of Geophysical Research*, *108*(A2), 1066. https://doi.org/10.1029/2002JA009493

Richmond, A. D., & Maute, A. (2014). Ionospheric electrodynamics modeling. In J. Huba, R. Schunk, & G. Khazanov (Eds.), *Modeling the ionosphere–thermosphere system*. https://doi.org/10.1002/9781118704417.ch6

Robinson, R. M., Vondrak, R. R., Miller, K., Dabbs, T., & Hardy, D. (1987). On calculating ionospheric conductances from the flux and energy of precipitating electrons. *Journal of Geophysical Research*, *92*, 2565–2569. https://doi.org/10.1029/JA092iA03p02565

Rodger, A. (2008). The mid-latitude trough—Revisited. In P. M. Kintner, Jr., A. J. Coster, T. Fuller-Rowell, A. J. Mannucci, M. Mendillo, & R. Heelis (Eds.), *Midlatitude ionospheric dynamics and disturbances*, *Geophysical Monograph Series* (Vol. 181, pp. 25–33). Washington, DC: American Geophysical Union.

Spiro, R. W., Heelis, R. A., & Hanson, W. B. (1978). Ion convection and the formation of the mid-latitude *F* region ionization trough. *Journal of Geophysical Research*, *83*, 4255–4264. https://doi.org/10.1029/JA083iA09p04255

Spiro, R. W., Wolf, R. A., & Fejer, B. G. (1988). Penetration of high-latitude electric-field effects to low latitudes during sundial 1984. *Annales de Geophysique*, *6*, 39–50.

Toffoletto, F., Sazykin, S., Spiro, R., & Wolf, R. (2003). Inner magnetospheric modeling with the Rice Convection Model. *Space Science Reviews*, *107*(1/2), 175–196. https://doi.org/10.1023/A:1025532008047

Tsyganenko, N. A., & Mukai, T. (2003). Tail plasma sheet models derived from Geotail particle data. *Journal of Geophysical Research*, *108*(A3), 1136. https://doi.org/10.1029/2002JA009707

Wang, H., Lühr, H., Häusler, K., & Ritter, P. (2011). Effect of subauroral polarization streams on the thermosphere: A statistical study. *Journal of Geophysical Research*, *116*, A03312. https://doi.org/10.1029/2010JA016236

Wang, H., Lühr, H., Ritter, P., & Kervalishvili, G. (2012). Temporal and spatial effects of subauroral polarization streams on the thermospheric dynamics. *Journal of Geophysical Research*, *117*, A11307. https://doi.org/10.1029/2012JA018067

Wang, H., Zhang, K., Zheng, Z., & Ridley, A. J. (2018). The effect of subauroral polarization streams on the mid-latitude thermospheric disturbance neutral winds: a universal time effect. *Annales Geophysicae*, *36*, 509–525. https://doi.org/10.5194/angeo-36-509-2018

Wolf, R. A. (1983). The quasi-static (slow-flow) region of the magnetosphere. In R. L. Carovillano & J. M. Forbes (Eds.), *Solar-terrestrial physics: Principles and theoretical foundations* (pp. 303–368). Norwell, MA: D. Reidel.

Yu, Y., Jordanova, V., Zou, S., Heelis, R., Ruohoniemi, M., & Wygant, J. (2015). Modeling subauroral polarization streams during the 17 March 2013 storm. *Journal of Geophysical Research: Space Physics*, *120*, 1738–1750. https://doi.org/10.1002/2014JA020371

Zhang, S.-R., Erickson, P. J., Foster, J. C., Holt, J. M., Coster, A. J., Makela, J. J., Noto, J., et al. (2015). Thermospheric poleward wind surge at midlatitudes during great storm intervals. *Geophysical Research Letters*, *42*, 5132–5140. https://doi.org/10.1002/2015GL064836

Zhang, X., Liu, L., & Liu, S. (2017). Dependence of thermospheric zonal winds on solar flux, geomagnetic activity, and hemisphere as measured by CHAMP. *Journal of Geophysical Research: Space Physics*, *122*, 8893–8914. https://doi.org/10.1002/2016JA023715

Zou, S., Ridley, A. J., Moldwin, M. B., Nicolls, M. J., Coster, A. J., Thomas, E. G., & Ruohoniemi, J. M. (2013). Multi-instrument observations of SED during 24–25 October 2011 storm: Implications for SED formation processes. *Journal of Geophysical Research: Space Physics*, *118*, 7798–7809. https://doi.org/10.1002/2013JA018860